Research Article Vol. 27, No. 20 / 30 September 2019 / *Optics Express* A1467

Optics EXPRESS

Design and demonstration of ultra-compact microcell concentrating photovoltaics for space

CHRISTIAN J. RUUD,[1] ALEX J. GREDE,[2] JAN-KAI CHANG,[3] MATTHEW P. LUMB,[4] KENNETH J. SCHMIEDER,[5] BRENT FISHER,[6] JOHN A. ROGERS,[3,7] JEFFREY M. GORDON,[8] AND NOEL C. GIEBINK[2,*]

[1] *Department of Materials Science and Engineering, The Pennsylvania State University, University Park, PA 16802, USA*
[2] *Department of Electrical Engineering, The Pennsylvania State University, University Park, PA 16802, USA*
[3] *Frederick Seitz Materials Research Laboratory, University of Illinois at Urbana-Champaign, Urbana, IL 61801, USA*
[4] *George Washington University, Washington, DC 20037, USA*
[5] *U.S. Naval Research Laboratory, Washington, DC 20375, USA*
[6] *H-NU Systems, LLC, Bethesda, MD 20817, USA*
[7] *Department of Materials Science and Engineering, Northwestern University, Evanston, IL 60208, USA*
[8] *Department of Solar Energy and Environmental Physics, Jacob Blaustein Institutes for Desert Research, Ben-Gurion University of the Negev, Sede Boqer Campus, 8499000, Israel*
[*] *ncg2@psu.edu*

Abstract: Optical concentration can improve the efficiency and reduce the cost of photovoltaic power but has traditionally been too bulky, massive, and unreliable for use in space. Here, we explore a new ultra-compact and low-mass microcell concentrating photovoltaic (µCPV) paradigm for space based on the monolithic integration of transfer-printed microscale solar cells and molded microconcentrator optics. We derive basic bounds on the compactness as a function of geometric concentration ratio and angular acceptance, and show that a simple reflective parabolic concentrator provides the best combination of specific power, angular acceptance, and overall fabrication simplicity. This architecture is simulated in detail and validated experimentally with a µCPV prototype that is less than 1.7 mm thick and operates with six, 650 µm square triple-junction microcells at a geometric concentration ratio of 18.4×. In outdoor testing, the system achieves a terrestrial power conversion efficiency of 25.8 ± 0.2% over a ±9.5° angular range, resulting in a specific power of approximately 111 W/kg. These results lay the groundwork for future space µCPV systems and establish a realistic path to exceed 350 W/kg specific power at >33% power conversion efficiency by scaling down to even smaller microcells.

1. Introduction

Modern space power systems employ multi-junction solar cells that deliver high efficiency (~30% at one-sun irradiance) and low mass but are expensive to produce (currently ~$100/W [1]). Overcoming this price-performance trade-off is a priority for both private space industries seeking to lower the cost of access to space, and for space agencies pursuing new missions that require high power for electric propulsion and/or operation in deep space [2]. Concentrating photovoltaic (CPV) systems have long been pursued to reduce the cost of power from multi-junction cells in terrestrial applications and have also been explored on a more limited basis in space [3–5]. However, despite the economic and efficiency advantages that CPV has to offer, particularly in the low intensity, low temperature (LILT) environment of deep space [6,7], conventional coverglass interconnected cell (CIC) assemblies remain the overwhelming choice for solar power onboard spacecraft.

#370182 https://doi.org/10.1364/OE.27.0A1467
Journal © 2019 Received 14 Jun 2019; revised 1 Aug 2019; accepted 3 Aug 2019; published 12 Sep 2019

To compete with CIC technology, CPV must be able to deliver its cost benefit without incurring an unacceptable mass, reliability, or optical loss penalty from the associated optics. Because concentration inherently limits the angular acceptance of the system according to the sine limit [8], any CPV system must also maintain its orientation toward the sun. While the pointing accuracy of many solar array wings is $<1°$ [9,10], the concentrator optics in a space CPV system must provide for a relatively large acceptance angle of $\pm 5°$ or more to accommodate potential errors, thermal distortion, and structural vibration. In typical communication and weather satellites, for example, the pointing accuracy is better than $\pm 1°$, whereas in star tracking satellites it might be as high as several thousandths of an arcsecond [11–14]. Past space CPV systems struggled to balance high concentration and angular tolerance in a compact, low-mass, and reliable form factor [4,5,15]. This was due in part to the size of traditional multi-junction PV cells (typically >1 cm^2), which naturally require larger and bulkier concentrator optics as well as advanced cell cooling to dissipate excessive heat.

The development of transfer-printed microscale multi-junction solar cells (typically defined as having an area <1 mm^2) opens the door to a new generation of space CPV systems that avoid many of these traditional drawbacks [16,17]. Scaling to sub-millimeter cell dimensions not only allows for dramatically more compact and low-mass concentrator optics (<1 mm thick), but also facilitates passive heat dissipation from the microcells themselves, which simplifies thermal management [18]. Operation in space, however, brings a unique set of constraints for CPV system design (moderate angular acceptance ~5° and 10–100× concentration ratio, minimum aspect ratio, and passive heat dissipation) that are much different than those that have historically guided the development of terrestrial CPV. Indeed, the demands of space CPV delegate the optical problem to a parameter space that appears not to have been of practical interest before, as the extremes of common interest until now have been either high concentration (up to ~1000×) and small angular acceptance $\leq 1°$ for terrestrial CPV, or low concentration ($\leq 3\times$) and large acceptance angle $>30°$ for stationary thermal concentrators. It has thus been unclear what concentrator design is optimal for a space μCPV system and what efficiency, specific power, and angular tolerance it might achieve in practice.

Here, we identify the fundamental and practical limits of the μCPV paradigm for space. We derive a relationship for how concentrator compactness depends on geometric concentration ratio and acceptance angle for μCPV, and show that a simple parabolic mirror ultimately provides the best overall combination of optical performance, fabrication tolerance, and low mass. We then experimentally demonstrate a proof-of-concept prototype with an array of triple-junction microcells monolithically bonded to a glass-filled mirror array 1 mm thick. Outdoor testing under the terrestrial solar spectrum achieves 25.8±0.2% power conversion efficiency at 18.4× geometric concentration with an acceptance angle of ±9.5°. These results establish a foundation for the design of ultra-compact μCPV systems and support the potential of this technology to improve performance and dramatically lower the cost of solar power in space.

2. Results

2.1. Limits of concentrator compactness

The critical importance of mass and compactness for space μCPV motivates the need for concentrator designs that minimize the areal mass density (kg/m^2) of the system. It is thus natural to ask whether there is a limit to concentrator compactness for a given geometric concentration ratio (CR) and acceptance half-angle (θ), since the sine limit dictates a trade-off between the latter two parameters [8] but does not place bounds on the physical size of the optical system. It is nevertheless clear from existing concentrator designs that compactness, as quantified by their axial length-to-aperture width aspect ratio (AR), can vary significantly while maintaining operation at the sine limit [8,19].

While a truly general bound on compactness is difficult to express, it is possible to derive a simple relationship for the minimum possible *AR* of a concentrator limited to a single refractive or reflective surface and a spatially uniform refractive index, which is the most practically-relevant situation for a μCPV system. The derivation follows from the geometric construction shown in Fig. 1(a), where an axisymmetric generic planar concentrator accepts all rays in the acceptance angle range $\pm\theta$ over the entrance aperture width $2u_{\mathrm{i}}$ and redirects them to the (downward-facing) receiver aperture, $2u_{\mathrm{o}}$. The compactness limit is then based on ensuring full angular acceptance from the extreme (rim) of the entry aperture, which also sets the maximum concentrator thickness (h) and thus the *AR* (in contrast to the practical geometric concentrators considered below, where *AR* is established by their apex region on the optic axis).

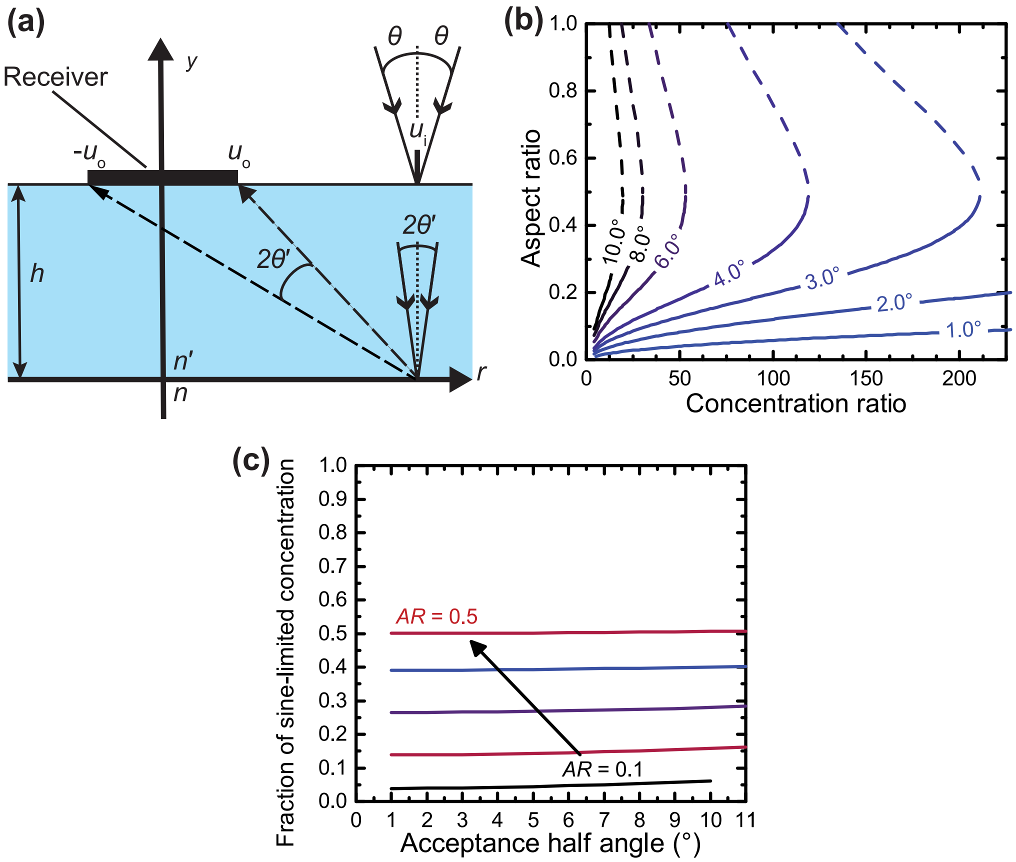

Fig. 1. (a) Diagram showing the geometry of a reflective single surface concentrator operating at the limit of compactness. (b) Trade-off between aspect ratio and concentration ratio for different acceptance half-angles (denoted by the contour labels) according to Eqn. 1. (c) Fraction of the sine-limiting concentration that can be achieved by an ideal reflective single surface concentrator with different aspect ratios.

The reflective surface (which might be a Fresnel reflector in practice, although the exact identity of the idealized optic is not required for deriving a bound on compactness) must conserve étendue at every point and therefore the angular wedge, $2\theta'$, subtended by the receiver at $r = u_{\mathrm{i}}$ on the reflective surface must be equal to the impinging wedge in the dielectric with refractive index n', which is related to the acceptance half-angle (θ) by Snell's law. Defining the concentration ratio, $CR \equiv (u_{\mathrm{i}}/u_{\mathrm{o}})^2$, and $AR \equiv h/2u_{\mathrm{i}}$, then leads to an implicit relationship among *AR*, *CR*, and

θ according to:

$$\tan^{-1}\left(\frac{1+\frac{1}{\sqrt{CR}}}{2AR}\right)-\tan^{-1}\left(\frac{1-\frac{1}{\sqrt{CR}}}{2AR}\right)=2\sin^{-1}\left(\frac{n}{n'}\sin\theta\right). \tag{1}$$

Figure 1(b) shows that there is an inherent trade-off between concentration ratio and compactness, which becomes more acute with increasing acceptance half-angle. The decline in concentration ratio at high AR indicated by the dashed portion of each contour occurs when the angle subtended by the receiver becomes limited by the concentrator height rather than the input aperture width and therefore is not meaningful. We note that an analogous concentrator with a refractive Fresnel lens surface focusing down onto a receiver cannot reach the bounds in Fig. 1(b) due to the limited refractive power of the dielectric (though an ideal diffractive metasurface could in principle [20]). It is also important to point out that the bound on CR from Eqn. 1 falls below the sine limit, which is easily appreciated from the fact that ray bundles incident at $r<u_\mathrm{i}$ do not fully fill the receiver and is a consequence of the single surface, uniform index restrictions imposed on the problem. Figure 1(c) quantifies this point by replotting Eqn. 1 as a fraction of the sine limit ($CR_\mathrm{max} = (n'\sin\theta_\mathrm{max}/n\sin\theta)^2$, where θ_max is the maximum ray half-angle on the receiver) for several constant AR values. Predictably, decreasing AR moves the system farther from sine-limiting operation, but nonetheless shows that there is no fundamental obstacle to realizing, for example, an ultralow $AR = 0.2$ µCPV system with concentration ratios $CR>35$ and an acceptance angle of $\theta = \pm5°$.

2.2. Ultra-compact concentrator designs

In practice, the idealized reflective surface underlying the limit above is difficult to fabricate at the millimeter scale relevant for µCPV and thus it is worthwhile to seek a geometric reflector that similarly minimizes the aspect ratio for a given CR and θ. As in Eqn. 1, specifying the acceptance angle defines the maximum angular wedge subtended by the receiver ($2\theta'$), which in turn sets both the position and slope of the reflector surface at the input aperture edge, $(r,\ y) = (u_\mathrm{i}, 0)$, as shown in Fig. 2(a). Moving in from this point (i.e., at positions $r<u_\mathrm{i}$), the reflector slope can be chosen to redirect ray 1 to the near edge of the receiver or ray 2 to the far edge of the receiver (but not both since $2\theta'$ no longer fully subtends the receiver), which ensures complete collection of light. The former option leads to a smaller slope (m_1) and thus to a lower AR optic whose form is determined from the differential Eq.:

$$\frac{dy}{dx}=m_1=\tan\left[\frac{1}{2}\left(\theta'+\tan^{-1}\left(\frac{r-u_\mathrm{o}}{h_\mathrm{edge}-y}\right)\right)\right]. \tag{2}$$

The edge thickness, h_edge, is determined from the relation $2\theta' + \tan^{-1}[(u_\mathrm{i} - u_\mathrm{o})/h_\mathrm{edge}] = \tan^{-1}[(u_\mathrm{i} + u_\mathrm{o})/h_\mathrm{edge}]$ and Eqn. 2 is solved over the domain $[0,\ u_\mathrm{i}]$.

The solution is a parabola with its axis tilted at angle θ' and its focus coinciding with the near edge of the receiver as illustrated by the red dashed line in Fig. 2(a). Joining this curve together with its mirror image on the other side of the y-axis thus yields an inverted compound parabolic concentrator (ICPC) as the minimum aspect ratio reflector for a given concentration ratio and acceptance angle. This result was originally obtained in [21] as a means to make terrestrial two-stage tailored edge ray concentrators more compact, though the ICPC solution in that case corresponds to solving the differential equation using the slope m_2 that maintains ray 2 at the far edge of the receiver. Figure 2(b) summarizes the performance of the ICPC from Eqn. 2 together with a simple parabolic reflector for comparison, where the optimal position of the receiver in

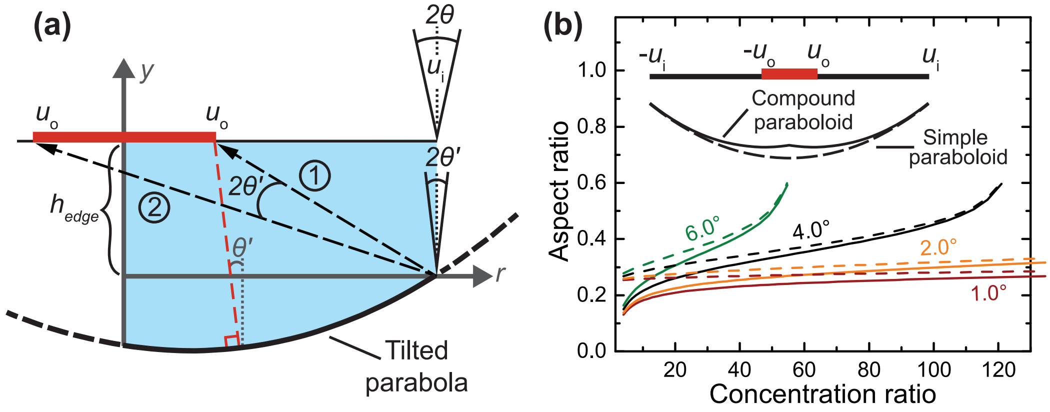

Fig. 2. (a) Construction of a single surface reflective concentrator with minimum aspect ratio for a given concentration ratio and acceptance angle, $\pm\theta$. The solution is a parabolic reflector with its axis tilted at θ' and its focus located at the near edge of the receiver; rotating the solid portion of this curve axisymmetrically about the y-axis defines the surface of the concentrator in three dimensions. (b) Comparison of simple and inverted compound parabolic concentrator designs for different acceptance half-angles. The inset illustrates the case of $CR = 25$ and $\theta = 4°$, where the compound parabolic design lowers the aspect ratio to $AR = 0.28$ compared with $AR = 0.32$ for the normal paraboloid.

the latter case is displaced slightly below the focal point by an amount:

$$\Delta y = u_i \cot\left[\tan^{-1}\left(\frac{u_i - \frac{u_i}{\sqrt{CR}}}{h_{edge}}\right) + \theta'\right]. \tag{3}$$

This plot shows that the ICPC aspect ratio converges with that of the simple parabola at high *CR* but can be substantially smaller in the low concentration, large acceptance angle regime relevant for space.

Ray tracing the 3D axisymmetric ICPC and simple parabola with Zemax OpticStudio leads to a different conclusion, however. Figure 3(a) shows a sample ray trace for both designs as well as a third, dual-mirror aplanatic concentrator that represents the state-of-the-art in compactness for terrestrial CPV [22–24]. Each of these systems is filled with dielectric ($n' = 1.5$) and is designed with the same concentration ratio ($CR = 25$), aspect ratio, and 4% shading loss incurred from the back of the cell (or the secondary in the aplanat case). Figure 3(b) shows the ideal optical efficiency simulated for each case assuming a solar disc half-angle of 0.27° and neglecting all absorption, reflection, and dispersion-related losses. Interestingly, although the ICPC has the highest nominal acceptance angle at ±7°, the softer efficiency decline of the simple paraboloid yields a larger practical acceptance angle, with >90% of the peak maintained to ±9.4° as compared to ±7.7° for the ICPC.

The acceptance angle is smaller in the aplanat case due to the limited numerical aperture of rays reaching the receiver set by the secondary. Moving the receiver up into the middle of the concentrator alleviates this problem (see Fig. 3(b), inset), but at the expense of lower optical efficiency due to ray blocking by the back side of the receiver. The slow initial efficiency decline in both cases stems from rays near the rim of the primary that miss the secondary, which is a consequence of the large entrance aperture set by the acceptance angle and the requirement of low shading [22]. These limitations are an example of the difficulty that can arise when attempting to adapt small angle, high *CR* terrestrial concentrator designs to the high angle, low concentration regime relevant for space.

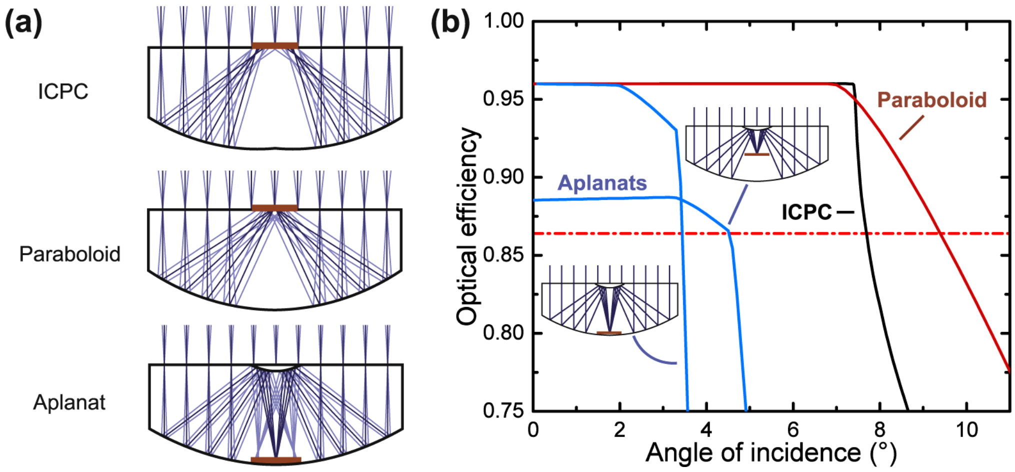

Fig. 3. (a) Ray tracing diagrams of the simple parabola, inverted compound parabolic concentrator (ICPC), and aplanatic concentrator designs. In the aplanatic system, light reflects off the parabolic primary surface to a secondary mirror which focuses the light back down onto the (upward-facing) receiver located at the vertex of the primary. Note, that the optimal position of the receiver in the simple paraboloid case is slightly below the nominal focal point as discussed in the text. (b) Simulated optical efficiency as a function of solar incidence angle for the the three concentrator designs in (a) operating at a common concentration ratio of $CR = 25$, 4% shading loss, and aspect ratio of $AR = 0.39$. The simulation is carried out assuming axisymmetric concentrators with dispersionless $n' = 1.5$ and no reflection or absorption losses. The horizontal red dashed line denotes 90% of the on-axis optical efficiency for the different designs.

These results motivate further exploration of the simple paraboloid design space in Fig. 4. There, we assume an axisymmetric paraboloid made of radiation-resistant glass ($n' = 1.5$ and mass density $\rho = 2.52\,\mathrm{g\,cm^{-3}}$ [25]) with a 170 μm diameter receiver placed optimally just below the focal point. The system is simulated ideally in the same manner as Fig. 3(a) and 3(b) and the resulting optical performance is plotted in terms of the optical efficiency per unit mass of the concentrator; the right-hand axis provides an estimate of the specific electrical power in space by scaling the curves with the AM0 solar flux and a constant η_{cell} =30% microcell efficiency. While the efficiency of state-of-the-art multi-junction cells can noticeably exceed 30% at 1 sun (and increases further with concentration) [26], we adopt the nominal value of 30% to maintain consistency in comparing with current space CIC cells.

The blue curves in Fig. 4 show the impact of varying the paraboloid edge thickness, which must be finite to form an arrayed concentrator optic in practice. All of the curves feature a specific power maximum that arises from the trade-off between optical efficiency loss from cell shading at low *CR* and mass increase at high *CR*. As the edge thickness increases, the maximum broadens and moves to higher concentration, suggesting an optimum *CR* range of roughly 8–30 for practical paraboloid-based μCPV systems.

In this context, it is instructive to compare the family of paraboloidal concentrators with the optimum lens-based concentrator, which does not suffer from cell shading loss and is indicated by the red dashed line. In this case, the optic is an ellipsoidal lens with the microcell embedded at its second focal point. Spherical aberration is eliminated by setting the ellipsoid eccentricity to $1/n'$ [8], from which it follows that the minimum aspect ratio is $AR = 1.1$ when $n' = 1.5$. This is over four times larger than the minimum for the paraboloidal concentrator ($AR = 0.25$). The difference stems fundamentally from the limited refractive power of the n to n' index discontinuity, which is

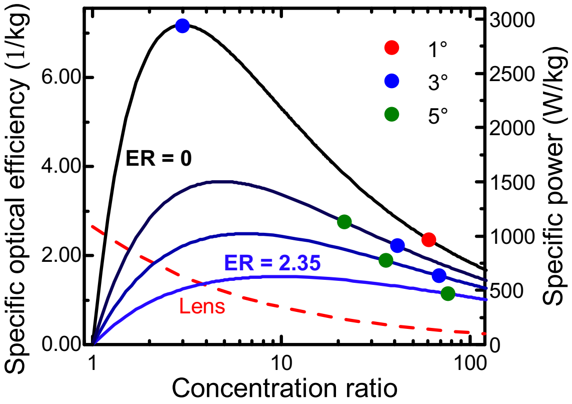

Fig. 4. Semi-log plot of specific optical efficiency simulated for an ideal reflective parabolic concentrator (solid lines) with different edge thicknesses specified via the ratio, ER, of edge thickness to receiver diameter. The colored dots mark different acceptance angles on each curve. The dashed red line is the result for an ellipsoidal refractive concentrator described in the text. The simulations are carried out with the same assumptions as Fig. 3(a) and 3(b). The right-hand axis rescales the data to specific power assuming a fixed 30% microcell efficiency and the AM0 solar flux of 1366 W m^{-2}.

the principal reason why refractive µCPV designs underperform their reflective counterparts in space applications.

2.3. Practical considerations

Beyond accounting for material absorption, dispersion, and Fresnel reflection losses, manufacturing constraints also influence the design of a practical µCPV system. Because the paraboloidal reflectors must be tiled in, for example, a hexagonal mirror array produced by precision glass molding techniques, there is a cusp loss between adjacent mirrors that becomes more significant as the system is miniaturized. In addition, a minimum array edge thickness (h_{edge}) is required to survive the glass molding process. Together, these factors bound the clear area (A) to mass (M) ratio of the concentrator optic according to:

$$\frac{A}{M} = \frac{48\left(\sqrt{3h_{\text{edge}}^2 + d^2} + \sqrt{3}h_{\text{edge}}\right)\left(\frac{\sqrt{3}}{2}\left(d - \frac{1}{2}w_{\text{cusp}}\right)^2 - w_{\text{cell}}^2\right)}{\rho\left[12d^2\left(\sqrt{3h_{\text{edge}}^2 + d^2} + \sqrt{3}h_{\text{edge}}\right)^2 - 5d^4\right]}, \tag{4}$$

where d is the pitch of the hexagonal array, ρ is the glass density, w_{cusp} is the cusp width between two adjacent mirrors, and w_{cell} is the side length of the square microcell. Neglecting absorption and reflection losses, Eqn. 4 sets the maximum specific power that can be achieved for a given glass molding process (which defines h_{edge} and w_{cusp}) and microcell technology (which defines w_{cell} and η_{cell}) assuming a parabolic concentrator design. Figure 5 shows the result of this calculation for state-of-the-art glass molding ($h_{\text{edge}} = 200$ µm and $w_{\text{cusp}} = 75$ µm) and nominal 30 %-efficient microcells with d varying implicitly to maximize the specific power. The key conclusion from this plot is that there is a limit to the benefits of cell miniaturization, with cell sizes below w_{cell} ~100 µm no longer leading to increased specific power.

Based on the results of Fig. 5, we select a 170 µm square microcell size and simulate the optical efficiency of a complete µCPV array in Fig. 6(a), fully accounting for fabrication constraints, material absorption, dispersion, and Fresnel reflection losses in the wavelength

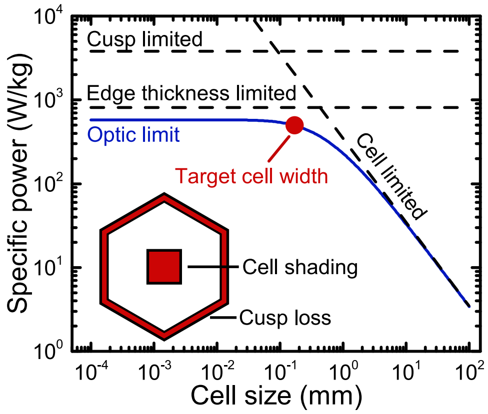

Fig. 5. Ideal specific power calculated for a hexagonal glass parabolic reflector array interfaced with square microcells according to Eqn. 4. In this log-log plot, h_{edge} = 200 µm, w_{cusp} = 75 µm, and the concentration ratio varies implicitly to maximize the specific power maintaining the same assumptions as in Fig. 4. In the limit of small cell size, the specific power becomes limited by the minimum thickness constraint of the optic before the cusp loss becomes dominant as indicated by the horizontal dashed lines.

range $300<\lambda<2000$ nm. Whereas the optical efficiency increases monotonically with *CR* due to the associated decrease in cell shading and cusp loss, the AM0 specific power shown on the right-hand axis peaks at ~380 W/kg for *CR* = 45. There is thus a trade-off between the maximum efficiency, specific power, angular acceptance, and cost reduction (i.e., concentration ratio) that must be weighed for a µCPV system depending on the nature of its mission. Assessing performance based only on a single metric, such as power conversion efficiency, would favor µCPV designs that are too massive and restrictive in their angular acceptance for many space power applications.

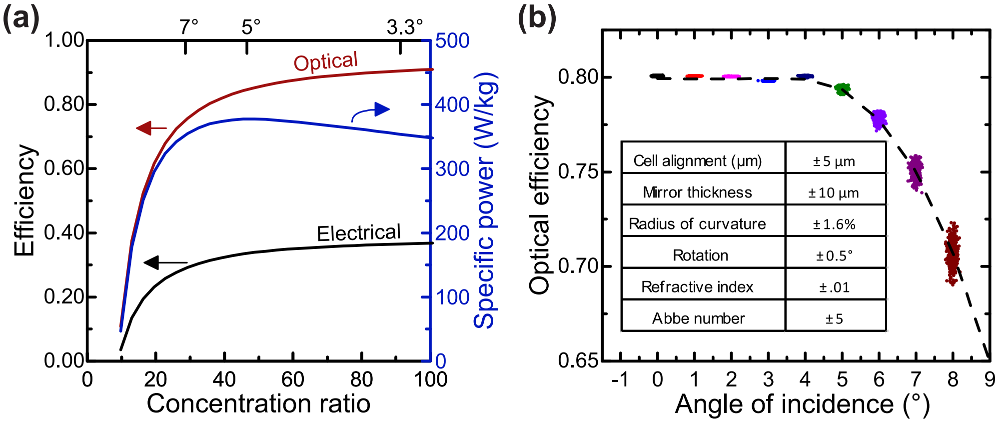

Cell alignment (µm)	±5 µm
Mirror thickness	±10 µm
Radius of curvature	±1.6%
Rotation	±0.5°
Refractive index	±.01
Abbe number	±5

Fig. 6. (a) Specific power simulated for a hexagonal µCPV array with 170 µm square microcells as shown in the inset. Acceptance half-angle (defined at 90% of the on-axis optical efficiency) is noted at the top of the plot. All optical losses and fabrication constraints are accounted for in the simulation. (b) Monte Carlo tolerance analysis expressing the spread in optical efficiency that results from random parameter variation within the tolerance ranges shown in the inset for the case of *CR* = 30.

The electrical efficiency in Fig. 6(a) largely follows the optical efficiency trend but also benefits from the intensity-dependent increase in microcell open-circuit voltage. The associated increase in microcell efficiency (which was not accounted for in Fig. 4 and Fig. 5) amounts to roughly 4% absolute per decade of concentration [26,27] and can easily offset the optical efficiency loss of the concentrator, enabling overall μCPV efficiencies >33% at the system level (corresponding to >39% efficiency at the individual microcell level [26]). Although the flux distribution delivered by the parabolic reflector is strongly inhomogeneous and would be of concern for large cells [28], previous work has shown that microscale solar cells are largely insensitive to such spatial variation [27]. Coupled with the robustness of the concentrator optic to typical manufacturing tolerances summarized in Fig. 6(b), it seems likely that μCPV could compete with or even surpass the absolute efficiency (~30%) and specific power (~ 200 W/kg) of existing multi-junction CIC technology [29].

2.4. Experimental prototype

To validate the parabolic μCPV design above, we implemented a proof-of-concept system shown in Fig. 7(a) based on a 12-cell array of 650 μm square triple junction InGaP/GaAs/InGaAsNSb microcells (designed for the AM1.5D terrestrial spectrum [26]) transfer-printed and interconnected on a 500 μm thick coverglass (Corning Eagle XG). Of the twelve cells, two strings of three series-connected cells were connected in parallel for electrical testing. The concentrator optic is a hexagonally tiled paraboloidal mirror array that is custom-molded in glass (Schott B 270) with a protected Ag mirror coating that provides ~96% average reflectivity over the solar spectrum. The pitch between adjacent hexagonal mirror cells is d = 3 mm and the maximum thickness of the optic is 1 mm, resulting in geometric concentration and aspect ratios of $CR = 18.4$ and $AR = 0.37$, respectively. The system is assembled by aligning and bonding the two components together with optical adhesive (NOA 63, Norland), resulting in a monolithic μCPV coupon with the microcells sandwiched in the middle (see Fig. 7(a)).

The system was subsequently tested outdoors on a clear sunny day at the National Oceanic and Atmospheric Administration Surface Radiation (NOAA SURFRAD) monitoring site located near State College, PA, which provides detailed minute-by-minute solar irradiance and weather data as described previously [30]. The μCPV coupon was mounted on a test fixture with a sundial to measure and controllably vary the solar incidence angle. Figure 7(b) shows the current-voltage characteristics collected for the μCPV coupon at normal incidence, which yields a power conversion efficiency of $\eta_{\mathrm{CPV}} = 25.8 \pm 0.2\%$ based on the direct normal irradiance incident on the system (see Fig. 7(b), inset). Varying the incidence angle by re-orienting the coupon sample results in the efficiency angular response shown in Fig. 7(c), which agrees well with that predicted by our Zemax ray tracing model.

The efficiency of the μCPV coupon is lower than that of the bare microcell array measured prior to assembly under similar irradiance conditions ($\eta_{\mathrm{PV}} = 31.5 \pm 0.2\%$ based on the global horizontal irradiance). The difference is due mainly to optical loss, which is detailed in the inset of Fig. 7(c) at normal incidence. The primary losses in this unoptimized prototype are cell and contact shading, Fresnel reflections, cusp losses, and material absorption. The net optical efficiency of the system is estimated to be 73 ± 2% by comparing the short-circuit current from the bare cell array to the CPV sample.

Efficiency loss due to microcell heating was previously observed in a similar μCPV system (70 K increase at a much higher concentration of ~740) [30] and is also a potential concern in space. Figure 8(a) displays the transient change in average cell temperature upon sudden exposure to direct sunlight based on the measured change in V_{oc} and its approximate temperature coefficient, $\beta_{\mathrm{cell}} \approx -4.7$ mV K^{-1} [30]. At steady-state, the open-circuit voltage of the μCPV array decreases by ~150 mV (this is the total for three cells in series), indicating that the temperature of each cell increases roughly 11 K above the ambient. The experimental results are accurately

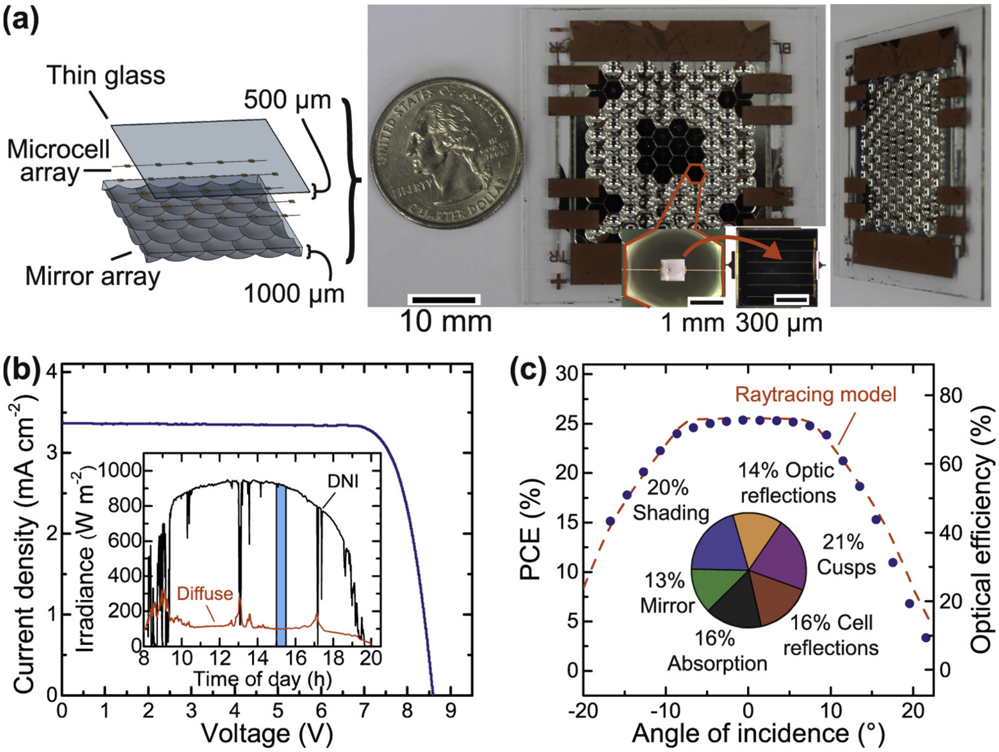

Fig. 7. The μCPV prototype is assembled from two components, i) a thin sheet of coverglass supporting the transfer-printed microcell array and ii) the reflective optic. Viewed on-axis, the image of the microcells is magnified and their associated mirror elements appear black; they appear reflective again when viewed off-axis beyond the angular tolerance of the system as shown in the right-most photograph. The smaller images in the middle show the backside of a cell after it has been bonded to the optics (left) and the front face of a typical microcell (right). (b) Current-voltage characteristic measured for the μCPV prototype outdoors on a clear sunny day, reflecting the output of two strings of three series-connected microcells; the current density is relative to the aperture area of the concentrator. The inset shows the direct (black) and diffuse (red) components of the solar spectrum on the day of the test; the measurements reported here were taken in the blue-highlighted window. (c) Power conversion efficiency (PCE) and optical efficiency measured outdoors as a function of incidence angle (blue circles) compared with that simulated by our ray tracing model (red dashed line). The factors that contribute to the optical loss at normal incidence are broken down in the inset pie chart. More than 95% of the shading loss in this case is due to the area of the cell with the remainder due to the metal interconnect traces. The relative loss contributions do not change significantly over the acceptance angle range of the concentrator.

described by a finite element model (dashed red line), where heat from the cell is conducted into the surrounding glass and ultimately removed from the system by convection and radiation. To simulate a space environment, the simulation is repeated in Fig. 8(b) for a purely radiative cooling regime, assuming 1366 W m^{-2} irradiance, an initial temperature of 173 K, and operation at open-circuit. The temperature increase is ~20% lower when the system is operated at its maximum power point due to the associated reduction in heat load.

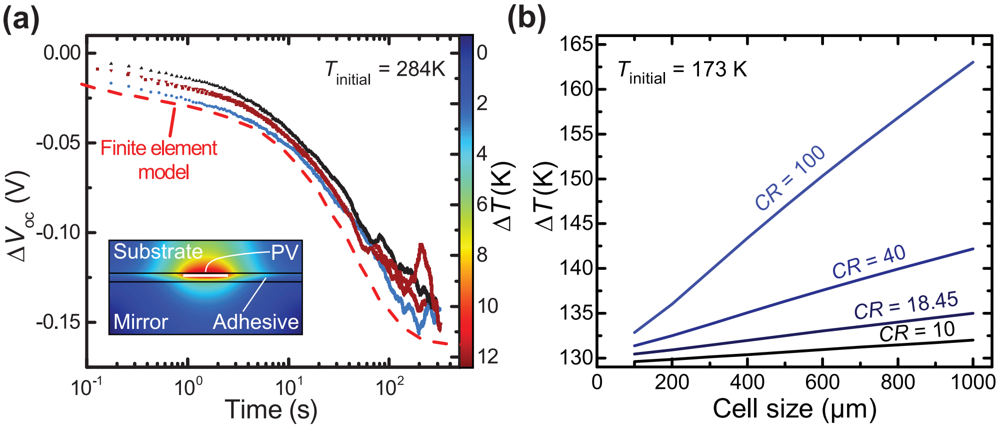

Fig. 8. (a) Transient change in V_{oc} measured by suddenly exposing the µCPV prototype to direct sunlight. The data are rescaled based on the known temperature coefficient of V_{oc} to reflect the change in average cell temperature on the right-hand axis, which agrees well with that predicted by a finite element heat transfer model indicated by the dashed red line. The inset shows a cross-section of the simulated temperature distribution at thermal equilibrium. (b) Microcell temperature predicted using the same model for a µCPV system operated in space at different concentration ratios, highlighting the passive cooling benefit of small microcell size.

3. Discussion

The efficiency and dimensions of the µCPV prototype above yield a specific power of ~111 W/kg based on the active area of the device and the AM0 spectrum. Scaling to smaller microcell sizes is a natural path to improvement following the trend in Fig. 5, though it is worth noting that cell perimeter recombination becomes more significant as cell size decreases. As an example, downsizing the same triple-junction microcells to 170 µm square and implementing them in the concentrator from Fig. 6(a) at a concentration ratio of 45 would be expected to yield a specific power >350 W/kg. Moving to smaller cells also further mitigates cell heating as evident from Fig. 8(b) and, because transfer printing enables different sub-cells to be mechanically stacked, there is a clear path to higher efficiency 5- and even 6-junction cells that are optimized for the AM0 spectrum [26,31].

The parabolic µCPV design chosen here is arguably the optimum for a single surface concentrator; however, adding a second, refractive surface could further improve the optical performance, with so-called RX and RXI designs that achieve sine limiting performance at $\theta = \pm 5°$ with aspect ratios of $AR = 0.38$ and $AR = 0.33$, respectively [8,23,32]. Such designs could in principle be implemented in a similar µCPV architecture as the prototype described here (i.e., microcells sandwiched between two molded optics) but would need to overcome additional transfer printing, interconnect patterning, and molded optic alignment challenges.

Reliability is an inevitable concern for any space µCPV system. Although we have not yet carried out radiation testing on our prototype, the microcells should benefit from a similar degree of radiation shielding as in conventional CICs since the same radiation-resistant coverglass and space-grade adhesive is used in both cases. Radiation shielding could even be enhanced in the µCPV case since additional metal shielding can be deposited on the back of the microcells (facing the sun) with minimal impact on the mass of the system. The reflective coating is not expected to degrade optically so long as it is deposited as a thin (<1 µm), dense layer using high quality starting materials [33–37]. Repeated thermal cycling in vacuum over a ±100 °C temperature range represents another critical test for this µCPV architecture, though the use of legacy materials with no thermal expansion mismatch between the bonded glass components at least holds the potential for high thermal stability.

The large-scale integration of many microcells (several thousand) in a µCPV coupon with the same size and form factor as a typical CIC represents both a potential reliability/yield risk and a potential opportunity. The opportunity stems from much greater circuit design freedom that could, for example, enable high voltage from a single µCPV coupon with many microcells connected in series. The impact of individual microcell failures, open- and short-circuit defects, and normal cell-to-cell electrical variation in large-scale µCPV arrays has been explored previously in [38–41]. In general, these studies conclude that optimal series/parallel interconnect strategies exist depending on the nature of the expected defects, and that robust performance can be achieved even without incorporating bypass diodes within an individual µCPV coupon.

Finally, as with any concentrator system [3,42], µCPV could be particularly beneficial for deep space missions since the available solar flux falls inversely with the square of the distance from the sun. The Juno spacecraft in orbit around Jupiter, for example, currently holds the record for most distant solar-powered spacecraft and operates with a solar flux that is ~25× lower than in Earth orbit. In such LILT conditions, shunt current and fill-factor losses can severely degrade PV performance [6,7] and thus the cells must be carefully optimized and individually screened [43]. By contrast, 25× µCPV concentration could restore the illumination intensity to around one sun and avoid the issue altogether, thus enabling new missions that push the limits of solar-powered exploration deeper into space.

4. Conclusion

In summary, we have detailed the design and prototype demonstration of a µCPV system for space solar power. We established the limits of concentrator performance and compactness for µCPV and determined that a reflective mirror array with parabolic mirrors provides the best overall combination of low mass, high optical efficiency, and high angular acceptance at concentration ratios in the range 25-50×. A proof-of-concept µCPV system was fabricated with triple junction microcells at 18.4× concentration and achieved 25.8% power conversion efficiency over an angular acceptance range of ±9.5° in terrestrial outdoor testing. These results provide a benchmark for future space µCPV systems, which could realistically exceed 350 W/kg and serve as a drop-in replacement for existing CIC technology at a substantially lower cost.

Funding

Advanced Research Projects Agency - Energy (DE-AR0000626); Air Force Research Laboratory (FA9453-17-C-0421); Israel Ministry of Science, Technology and Space (Grant number 3-15970).

References

1. K. A. W. Horowitz, T. W. Remo, B. Smith, and A. J. Ptak, "A techno-economic analysis and cost reduction roadmap for III-V solar cells" (National Renewable Energy Laboratory, 2018), NREL/TP-6A20-72103.
2. "NASA Technology Roadmaps - TA 3 Space Power and Energy Storage" (National Aeronautics and Space Administration, 2015), pp. 12–16
3. M. O'Neill, A. J. McDanal, H. Brandhorst, K. Schmid, P. LaCorte, M. Piszczor, and M. Myers, "Recent space PV concentrator advances: More robust, lighter, and easier to track," in *2015 IEEE 42nd Photovoltaic Specialist Conference (PVSC)* (IEEE, 2015), pp. 1–6.

4. M. O'Neill, A. J. McDanal, M. Piszczor, T. Peshek, M. Myers, C. McPheeters, J. Steinfeldt, B. Heintz, P. Sharps, M. Puglia, and C. Kumar, "Advanced development of space photovoltaic concentrators using robust lenses, multi-junction cells, & graphene radiators," in *2018 IEEE 7th World Conference on Photovoltaic Energy Conversion (WCPEC) (A Joint Conference of 45th IEEE PVSC, 28th PVSEC 34th EU PVSEC)* (IEEE, 2018), pp. 3378–3383.
5. M. Eskenazi, A. Jones, R. K. Jain, B. Hoang, K. MacDonald, Y. N. Wong, J. Kesapradist, and G. V. Ommering, "Preliminary test results for the CellSaver concentrator in geosynchronous earth orbit," in *Conference Record of the Thirty-first IEEE Photovoltaic Specialists Conference, 2005* (IEEE, 2005), pp. 622–625.
6. R. Hoheisel, R. J. Walters, and A. W. Bett, "Low temperature effects in photovoltaic devices for deep space missions," in *2015 IEEE 42nd Photovoltaic Specialist Conference (PVSC)* (IEEE, 2015), pp. 1–5.
7. R. Hoheisel, A. W. Bett, J. H. Warner, R. J. Walters, and P. P. Jenkins, "Low temperature low intensity effects in III-V photovoltaic devices for deep space missions," in *2018 IEEE 7th World Conference on Photovoltaic Energy Conversion (WCPEC) (A Joint Conference of 45th IEEE PVSC, 28th PVSEC 34th EU PVSEC)* (IEEE, 2018), pp. 3763–3767.
8. R. Winston, J. C. Miñano, P. Benítez, N. Shatz, and J. C. Bortz, *Nonimaging Optics* (Elsevier, 2005).
9. M. Perry, P. Alea, M. Cully, M. McCullough, P. Sanneman, N. Teti, and B. Zink, "Earth Observing-1 Spacecraft Bus," in *Proceedings of the 15th Annual AIAA/USU Conference on Small Satellites* (IEEE, 2001), SSC01-V-6.
10. B. R. Clapp, H. J. Weigl, N. E. Goodzeit, D. R. Carter, and T. J. Rood, "GOES-R active vibration damping controller design, implementation, and on-orbit performance," CEAS Space J. **10**(4), 501–517 (2018).
11. G. M. Lerner, "Attitude Hardware," in Spacecraft Attitude Determination and Control, J. R. Wertz, ed. (Springer Netherlands, 1978).
12. F. L. Markley and J. L. Crassidis, *Fundamentals of spacecraft attitude determination and control* (Springer, 2014), Chap. 7.
13. P. A. Jones and B. R. Spence, "Spacecraft solar array technology trends," in *1998 IEEE Aerospace Conference Proceedings (Cat. No.98TH8339)* (IEEE, 1998), pp. 141–152
14. D. M. Allen, P. J. Jones, D. M. Murphy, and M. F. Piszczor, "The SCARLET light concentrating solar array," in *Conference Record of the Twenty Fifth IEEE Photovoltaic Specialists Conference - 1996* (IEEE, 1996), pp. 353–356.
15. J. S. Fodor, M. A. Frey, S. W. Gelb, Z. Maassarani, J. S. Powe, and J. A. Schwartz, "In-orbit performance of space solar arrays," in *3rd World Conference on Photovoltaic Energy Conversion, 2003. Proceedings of* (IEEE, 2003), pp. 638–641.
16. M. P. Lumb, B. Fisher, K. J. Schmieder, and M. Meitl, "Six-junction (6J) microscale concentrating photovoltaics (CPV) for space applications," in *2016 IEEE 43rd Photovoltaic Specialists Conference (PVSC)* (IEEE, 2016), pp. 3415–3420.
17. Matt Lumb, "Sending CPV into Space," Compd. Semicond. **24**(8), 36–40 (2018).
18. C. J. Ruud, J. S. Price, B. Fischer, B. Wang, and N. Giebink, "Lightweight monolithic microcell CPV for space," in *2018 IEEE 7th World Conference on Photovoltaic Energy Conversion (WCPEC) (A Joint Conference of 45th IEEE PVSC, 28th PVSEC & 34th EU PVSEC)* (IEEE, 2018), pp. 3535–3538.
19. J. Chaves and M. Collares-Pereira, "Ultra flat ideal concentrators of high concentration," Sol. Energy **69**(4), 269–281 (2000).
20. N. Yu, P. Genevet, M. A. Kats, F. Aieta, J. Tetienne, F. Capasso, and Z. Gaburro, "Light propagation with phase discontinuities: Generalized laws of reflection and refraction," Science **334**(6054), 333–337 (2011).
21. R. P. Friedman, J. M. Gordon, and H. Ries, "Compact high-flux two-stage solar collectors based on tailored edge-ray concentrators," Sol. Energy **56**(6), 607–615 (1996).
22. J. M. Gordon and D. Feuermann, "Optical performance at the thermodynamic limit with tailored imaging designs," Appl. Opt. **44**(12), 2327–2331 (2005).
23. R. Winston and J. M. Gordon, "Planar concentrators near the étendue limit," Opt. Lett. **30**(19), 2617–2619 (2005).
24. A. Goldstein, D. Feuermann, G. D. Conley, and J. M. Gordon, "Nested aplanats for practical maximum-performance solar concentration," Opt. Lett. **36**(15), 2836–2838 (2011).
25. K. Eichgrün, "Technical Safety Information BK7G18" (Schott AG, 2015). https://www.schott.com/d/advanced˙optics/248e1947-ddc0-4245-907b-4cb890a44439/BK7G18˙SDS˙EN˙V5˙201505.pdf.
26. X. Sheng, C. A. Bower, S. Bonafede, J. W. Wilson, B. Fisher, M. Meitl, H. Yuen, S. Wang, L. Shen, A. R. Banks, C. J. Corcoran, R. G. Nuzzo, S. Burroughs, and J. A. Rogers, "Printing-based assembly of quadruple-junction four-terminal microscale solar cells and their use in high-efficiency modules," Nat. Mater. **13**(6), 593–598 (2014).
27. O. Korech, B. Hirsch, E. A. Katz, and J. M. Gordon, "High-flux characterization of ultrasmall multijunction concentrator solar cells," Appl. Phys. Lett. **91**(6), 064101 (2007).
28. H. Baig, K. C. Heasman, and T. K. Mallick, "Non-uniform illumination in concentrating solar cells," Renewable Sustainable Energy Rev. **16**(8), 5890–5909 (2012).
29. D. Wilt, S. Messenger, and A. Howard, "Technology opportunities to enable high mass specific power," in *2009 34th IEEE Photovoltaic Specialists Conference (PVSC)* (IEEE, 2009), pp. 001500–001506.
30. J. S. Price, A. J. Grede, B. Wang, M. V. Lipski, B. Fisher, K.-T. Lee, J. He, G. S. Brulo, X. Ma, S. Burroughs, C. D. Rahn, R. Nuzzo, J. A. Rogers, and N. C. Giebink, "High-concentration planar microtracking photovoltaic system exceeding 30% efficiency," Nat. Energy **2**(8), 17113 (2017).

31. M. P. Lumb, S. Mack, K. J. Schmieder, M. González, M. F. Bennett, D. Scheiman, M. Meitl, B. Fisher, S. Burroughs, K.-T. Lee, J. A. Rogers, and R. J. Walters, "GaSb-Based solar cells for full solar spectrum energy harvesting," Adv. Energy Mater. **7**(20), 1700345 (2017).
32. J. C. Miñano, P. Benítez, and J. C. González, "RX: a nonimaging concentrator," Appl. Opt. **34**(13), 2226–2235 (1995).
33. I. D. Sarcina, M. L. Grilli, F. Menchini, A. Piegari, S. Scaglione, A. Sytchkova, and D. Zola, "Behavior of optical thin-film materials and coatings under proton and gamma irradiation," Appl. Opt. **53**(4), A314–A320 (2014).
34. R. Schnadt and J. Schneider, "The electronic structure of the trapped-hole center in smoky quartz," Eur. Phys. J. B **11**(1), 19–42 (1970).
35. R. D. Aines and G. R. Rossman, "Relationships between radiation damage and trace water in zircon, quartz, and topaz," Am. Mineral. **71**(9-1), 1186–1193 (1986).
36. J. D. Barrie, M. J. Meshishnek, P. D. Fuqua, and W. C. Rostel, "Simulated space environmental exposure of optical coatings for spacecraft solar rejection," Appl. Opt. **41**(16), 3150–3155 (2002).
37. S. F. Pellicori, C. L. Martinez, P. Hausgen, and D. Wilt, "Development and testing of coatings for orbital space radiation environments," Appl. Opt. **53**(4), A339–A350 (2014).
38. J. E. Moore, K. J. Schmieder, W. Wagner, and M. P. Lumb, "Strategies for defect-tolerant microconcentrator photovoltaic modules," J. Photonics Energy **9**(01), 014501 (2019).
39. A. L. Lentine, G. N. Nielson, M. Okandan, W. C. Sweatt, J. L. Cruz-Campa, and V. Gupta, "Optimal cell connections for improved shading, reliability, and spectral performance of microsystem enabled photovoltaic (MEPV) modules," in *2010 35th IEEE Photovoltaic Specialists Conference* (IEEE, 2010), pp. 003048–003054.
40. E. Menard, W. Wagner, B. Furman, K. Ghosal, J. Gabriel, M. Meitl, and S. Burroughs, "Multi-physics circuit network performance model for CPV modules/systems," in *2011 37th IEEE Photovoltaic Specialists Conference* (IEEE, 2011), pp. 002268–002272.
41. A. L. Lentine, G. N. Nielson, M. Okandan, J. Cruz-Campa, and A. Tauke-Pedretti, "Voltage matching and optimal cell compositions for microsystem-enabled photovoltaic modules," IEEE J. Photovolt. **4**(6), 1593–1602 (2014).
42. D. M. Murphy and D. M. Allen, "SCARLET development, fabrication, and testing for the Deep Space 1 spacecraft," in *IECEC-97 Proceedings of the Thirty-Second Intersociety Energy Conversion Engineering Conference (Cat. No.97CH6203)* (American Institute of Chemical Engineers, 1997), pp. 2237–2245.
43. S. F. Dawson, P. Stella, W. McAlpine, and B. Smith, "JUNO Photovoltaic power at Jupiter," in *10th International Energy Conversion Engineering Conference* (American Institute of Aeronautics and Astronautics, 2012), pp. 2012–3833.